

Magnetoresistance anisotropy of polycrystalline cobalt films: Geometrical-size and domain effectsWoosik Gil,¹ Detlef Görlitz,¹ Michael Horisberger,² and Jürgen Kötzer¹¹*Institut für Angewandte Physik und Zentrum für Mikrostrukturforschung, Universität Hamburg, Jungiusstrasse 11, D-20355 Hamburg, Germany*²*ETH Zürich & Paul Scherrer Institut, CH-5232 Villigen PSI, Switzerland*

(Received 20 May 2005; revised manuscript received 22 July 2005; published 3 October 2005)

The magnetoresistance (MR) of 10–200 nm thin polycrystalline Co-films, deposited on glass and insulating Si(100), is studied in fields up to 120 kOe, aligned along the three principal directions with respect to the current: Longitudinal, transverse (in-plane), and polar (out-of-plane). At technical saturation, the anisotropic MR (AMR) in polar fields turns out to be up to twice as large as in transverse fields, which resembles the yet unexplained geometrical size-effect (GSE), previously reported for Ni- and Permalloy films. Upon increasing temperature, the polar and transverse AMR's are reduced by phonon-mediated sd-scattering, but their ratio, i.e., the GSE remains unchanged. Basing on Potters's theory [Phys. Rev. B **10**, 4626 (1974)], we associate the GSE with an anisotropic effect of the spin-orbit interaction on the sd-scattering of the minority spins due to a film texture. Below magnetic saturation, the magnitudes and signs of all three MR's depend significantly on the domain structures depicted by magnetic force microscopy. Based on hysteresis loops and taking into account the GSE within an effective medium approach, the three MR's are explained by the different magnetization processes in the domain states. These reveal the importance of in-plane uniaxial anisotropy and out-of-plane texture for the thinnest and thickest films, respectively.

DOI: [10.1103/PhysRevB.72.134401](https://doi.org/10.1103/PhysRevB.72.134401)

PACS number(s): 73.50.-h, 73.50.Jt, 73.61.-r, 75.47.-m

I. INTRODUCTION

In applied magnetism, the coupling of the magnetic moment to spatial degrees of freedom plays a key role, and this especially applies to modern magneto- or spin-electronics.¹ Basically, this coupling is provided by the spin-orbit interaction, which in the example of magnetotransport causes the scattering rate of the conduction electrons, τ^{-1} , to depend on the direction of the local magnetization \mathbf{M} with respect to the current. In the archetypal bulk ferromagnets iron, cobalt, nickel, and their alloys, the resistance difference for orientations of \mathbf{M} parallel and perpendicular to the current, i.e., the so-called anisotropic magnetoresistance ratio (AMR), $\Delta\rho/\rho \equiv 3(\rho_{\parallel} - \rho_{\perp})/(\rho_{\parallel} + 2\rho_{\perp})$, amounts to some percent. In nanostructured devices like magnetic multilayers, wires, or constrictions in the ballistic regime,² this ratio may be enhanced to several ten percent.

Basically, the determination of the scattering rate $\tau^{-1}(\mathbf{M})$ and of the AMR requires the knowledge of the scattering potential and also of the spin-orbit split bands at the Fermi-surface ϵ_F . Some special aspects of the AMR have been evaluated by Smit,³ Berger,⁴ Potter,⁵ and Fert and Campbell,⁶ however, the evaluation of $\tau^{-1}(\mathbf{M})$ for a realistic case is still lacking, at least to the best of our knowledge. In this context, we note a recent *ab initio* calculation of the intrinsic anomalous Hall-effect which, in contrast to the AMR, depends only to first order on the spin-orbit interaction and *not* on a scattering potential. This quantity was obtained by integrating the k -space Berry-phase over the occupied spin-orbit split states of iron⁷ and was found to agree up to some 30 percent with data on iron whiskers.⁸

The present work is intended to a fairly systematic study of the AMR, which is of second-order in the spin-orbit interaction, also in an elemental 3d-ferromagnet. By selecting hcp cobalt with a rather well known band-structure,⁹ some deeper

insight into the AMR may be facilitated. By choosing polycrystalline films, we are closer to devices which invariably use polycrystalline materials. We will vary the structural disorder and the temperature in the films to probe the role of different scattering mechanisms. These basic properties of the films under study are examined in Sec. II. Section III is devoted to the AMR in the technically saturated state with main emphasis to a still unexplained phenomenon of the AMR, i.e., the so-called geometrical-size effect (GSE), previously observed in thin Ni¹⁰ and Permalloy¹¹ films. Another point of interest will be the absolute value of $\Delta\rho$ at low temperatures: For Ni-alloys, already McGuire and Potter¹² pointed out the unsensitivity of $\Delta\rho$ against significant variations of the residual resistivity $\rho(0)$. The influence of different domain structures, depending on the film thicknesses, on the magnetoresistance, is investigated in Sec. IV and will be discussed by using the results on the GSE. This low-field regime, where the in-plane AMR switches at rather small coercive fields ($H_c \approx 10$ Oe), may be of interest for applications despite the fact that $\Delta\rho/\rho$ lies in the range of some percent. The summary and conclusions are contained in Sec. V.

II. CHARACTERIZATION OF THE FILMS

By means of DC-magnetron sputtering at an Ar-pressure of $2 \cdot 10^{-9}$ bar, cobalt films of thicknesses 10, 20, and 188 nm were deposited on Synsil-glass and oxidized Si(100) surfaces and capped by 3 nm thick Al-layers. The thicknesses were measured by a profilometer to an accuracy of 0.6 nm and confirmed by determining the magnetic moments using a high-resolution SQUID (Quantum Design, MPMS2). X-ray diffraction diagrams (XRD), as shown in Fig. 1, revealed a polycrystalline hcp-structure with a slight texture of the hexagonal axis normal to the plane. Surface images recorded by

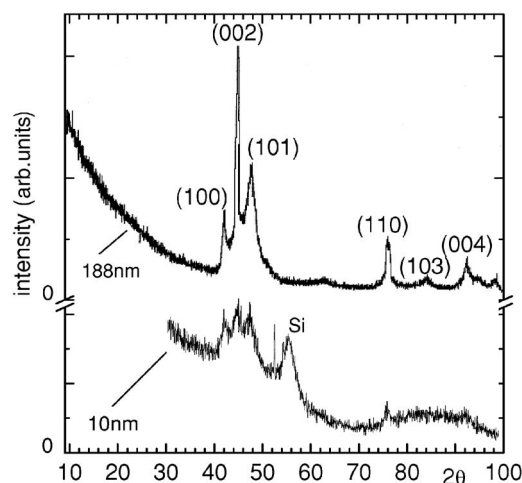


FIG. 1. Wide-angle X-ray diffraction patterns of Co-films deposited by DC-magnetron sputtering on glass (188 nm) and on oxidized Si (100) (10 nm). The Miller indices (hkl) denote the reflections expected for the hcp structure at incident wavelength $\lambda_{CuK\alpha} = 1.54 \text{ \AA}$.

an atomic force microscope (AFM, Q-ScopeTM250, Quesant Instruments Co.) yielded surface roughnesses between $(1.5 \pm 0.3) \text{ nm}$ for 10 nm and $(3.8 \pm 0.5) \text{ nm}$ for 188 nm and indicated the grain sizes to increase from $(25 \pm 5) \text{ nm}$ to $(80 \pm 5) \text{ nm}$. Within the error margins, these results turned out to be the same for both substrates. It is interesting to note that the grain sizes and their increase with thickness are consistent with a recent report for polycrystalline Co on glass and Si(100) substrates.¹³

The magnetic properties of all films have been investigated by ferromagnetic resonance (FMR), hysteresis loops, and magnetic force microscopy (MFM). Using a homemade FMR spectrometer operating at 9.1 GHz, the directions and magnitudes of small uniaxial anisotropy fields, \mathbf{H}_u , in the film planes were determined. On 20 nm Co:Si and 188 nm Co:glass, for example, $H_u = 22.3$ and 15.3 Oe , respectively, was obtained and the orientation of \mathbf{H}_u could be related to the direction of the deposition process. Magnetization isotherms were measured by a SQUID-magnetometer (Quantum Design MPMS2) along three orthogonal directions of the applied field \mathbf{H} at temperatures, which were of interest for the analyses of the magnetoresistances (MR's) in Sec. IV. There also MFM images are presented in order to visualize the domain structure underlying the magnetization processes, see Fig. 7 below. For this purpose, the Q-scope was equipped with a commercial tip, coated by a 40 nm thin hard Co-alloy (NanosensorsTM), and magnetized perpendicularly to the scanning directions. The directions of the in-plane magnetization were determined by monitoring the domain wall motion induced by a small magnetic field produced by external Helmholtz coils.

The resistances have been measured by an array of four in-line contacts prepared parallel to \mathbf{H}_u by ultrasonic bonding. The driving currents were kept small enough to produce linear responses and the resulting UII -ratios were corrected for the sample geometry¹⁴ to determine the resistivities of the films. The sample chip was mounted to the end of an cold-

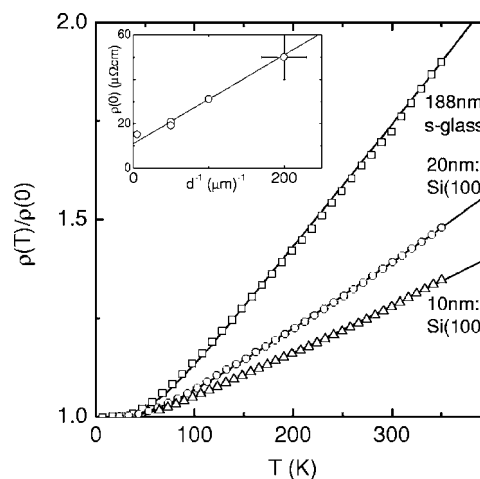


FIG. 2. Temperature variation of the zero-field resistance of the three Co-films under study. The solid line represents a fit to Eq. (1), taking into account the contributions by phonon-mediated sd - and electron-magnon scattering. Inset: Linear dependence of the residual resistivity on the inverse thickness d , including a result for $d=5 \text{ nm}$ from Ref. 5.

finger extending from the cold-plate of a pulse-tube cooler (PRK, Transmit Co. Giessen, Germany) to the center of a warm-bore superconducting magnet (130 kOe, Oxford Instruments). A PID controller and a heater allowed stable sample temperatures between 70 and 350 K. Measurements of the magnetoresistance in the domain states, i.e., at low magnetic fields, were performed by means of an electromagnet, by which also the angle between current and field could be varied. More experimental details are given in Ref. 15. We should mention here, that the structural, magnetic, and transport properties proved to be largely independent on the substrate, i.e., synsil-glass or oxidized Si(100).¹⁵ This feature indicates a dominant effect of the polycrystallinity of the films, i.e., of the deposition process. For some practical reasons, we selected three films with thicknesses between 10 and 188 nm for the present study.

The temperature dependence of the zero-field resistivities is depicted in Fig. 2 for these three films. The data can be well described by a sum of three contributions

$$\rho(T) = \rho(0) + \rho_{ph}(T) + \rho_m(T). \quad (1)$$

According to the inset, the residual resistivity increases linearly with the inverse thickness,

$$\rho(0) = \rho_b(0)[1 + d_c/d],$$

defining a bulk value, $\rho_b(0) = (11 + 1) \mu\Omega\text{cm}$, and a characteristic thickness, $d_c = (18 \pm 1) \text{ nm}$. Existing theories on extra scattering by the film surfaces¹⁶ or grain boundaries¹⁷ predict such $1/d$ -behavior only for small deviations from the bulk limit, $d > d_c$, so that the observed increase of $\rho(0)$ indicates scattering by an additional, yet unidentified disorder in the thinner films. Using $\rho_b(0)$, the carrier density $5.8 \cdot 10^{22} \text{ cm}^{-3}$ from Hall-data for these films,¹⁵ and the free electron model for the conduction electrons in Co,¹⁸ we find an upper limit for the mean free path, $\ell_e(0) = \hbar k_F / n_e e^2 \rho_b(0) \approx 11 \text{ nm}$. Since

this length is significantly smaller than the mean grain sizes observed by AFM, it may be associated with point-defect scattering within the otherwise crystalline grains.

Since the electron-magnon scattering in Co, $\rho_m(T) = 1.5 \cdot 10^{-5} (\mu\Omega\text{cm K}^{-2}) T^{2.19}$ is small, the temperature variation of the resistivities should be dominated by phonons. Indeed, by fitting $\rho(T)$ to the Bloch-Grueneisen form

$$\rho_{ph}(T) = \rho_{ph} \cdot \left(\frac{T}{\Theta_D} \right)^n \int_0^{\Theta_D/2T} \frac{x^n}{(\sinh x)^2} dx$$

and taking for the Debye temperature $\Theta_D = 445$ K, we find an excellent agreement by setting for the exponent $n=3$, valid for phonon-mediated sd-scattering.^{20,21} The strength of this scattering, increases from $\rho_{ph} = (90 \pm 6) \mu\Omega\text{cm}$ in the two thinner, more disordered films to $142 \mu\Omega\text{cm}$ in the thickest film. However, due to coupling of the phonons to the complicated structure of the d -states, it is difficult to estimate ρ_{ph} even for single crystals.²¹

Finally, it may be interesting to note that the present resistivities of the 188 nm film are almost identical to those obtained by Freitas *et al.*²² on a 300 nm Co film deposited by magnetron sputtering on glass. This applies to the residual resistivity, $\rho(0) = 14 \mu\Omega\text{cm}$, as well as to $\rho(T)$ at room temperature. Significantly smaller $\rho(0)$ -values have been detected on diode sputtered²² and epitaxial²³ films of similar thickness.

III. HIGH-FIELD MAGNETORESISTANCE

The MR of all films has been studied for three principal directions of \mathbf{H} , defined by the directions of the current ($\mathbf{I} \parallel \mathbf{H}_u$) and the film plane, see inset to Fig. 3(a). To give an example, Fig. 3(a) shows the three MR's of the 20 nm film at room-temperature. Starting from a common value at low fields, a negative MR is found for all directions of \mathbf{H} . While the longitudinal MR, $\rho(H_\ell)$ decreases linearly with field, the transverse and polar MR's contain additional contributions. Above the saturation fields H_s , where the films become homogeneously magnetized, $\mathbf{M}(H > H_s) = M_s \mathbf{H}/H$, these additional contributions to the MR also saturate at values $\Delta\rho_t = \rho_\ell - \rho_t$ and $\Delta\rho_p = \rho_\ell - \rho_p$, both indicated in Fig. 3(a). This contribution results from the spin-orbit induced AMR, since upon rotation of the magnetization either to the transverse or to the polar direction, we realize the angular dependence

$$\rho(\varphi) = \rho(0) - \Delta\rho \cdot \sin^2 \varphi, \quad (2)$$

where φ is the angle between current and the direction of the magnetization \mathbf{M} . Such behavior is characteristic of the AMR of polycrystalline samples of cubic or hexagonal ferromagnets,¹² and is illustrated by Fig. 3(b) for the in-plane rotation of \mathbf{M} in a field $H = 0.6 \text{ kOe} > H_s$. Details of the MR during saturation by (weak) *in-plane* fields will be discussed in Sec. IV. Here we look at the *polar* MR by increasing H_p in Fig. 3(a). SQUID magnetization data¹⁵ reveal $M_p(H_p < M_s) = H_p$ due to a rotation of \mathbf{M} against the in-plane demagnetizing field $H_N = -M_s$, so that the angle between \mathbf{M} and current $\mathbf{I}(\parallel \mathbf{H}_u)$ is determined by $\sin \varphi = M_p/M_s = H_p/M_s$. For this case, Eq. (2) predicts a parabolic decrease, $\rho(H_p) - \rho(0) =$

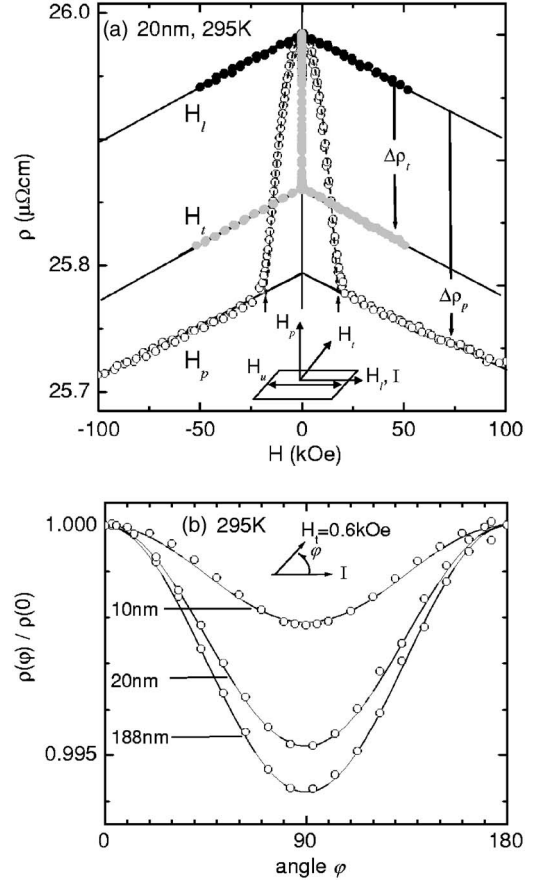


FIG. 3. (a) High-field magnetoresistance (MR) of the 20 nm Co-film at room temperature for the three principal directions of the field (see inset), revealing the transverse and polar MR's, $\Delta\rho_t$ and $\Delta\rho_p$, and the appearance of a linear negative MR at $M > M_s$. The dashed curve through the polar MR-data presents a fit to Eq. (2). (b) Normalized in-plane MR of Co-films, $\rho(\varphi)/\rho(0)$, recorded at room temperature as a function of the angle φ between current and field above the saturation field of the in-plane magnetization. The solid curves represent fits to Eq. (2) valid for the anisotropic MR (AMR).

$-\Delta\rho_p(H_p/M_s)^2$, which is depicted in Fig. 3(a) by the dashed curve in full agreement with the data.

A. Spin-wave contribution

It is evident from Fig. 3(a) that the linear MR, $d\rho/dH$, is the same in all directions of \mathbf{H} . No signature of the classical Lorentz-MR, which is positive and proportional to $(M+H)^2$, is realized for $H > H_s$, even not at room temperature. Due to the small mean free path the absence of this effect is plausible, while in epitaxial films it becomes visible.²³ The linear MR has been realized before in $\rho(H_\ell)$ on epitaxially grown iron, cobalt, and nickel films on MgO and Al_2O_3 ¹⁹ and was quantitatively discussed in terms of elastic scattering by thermally excited magnons. Roughly spoken, the negative MR can be ascribed to the suppression of low energy magnons, which results from the increase of the magnon gap proportional to H . The strong thermal increase of $d\rho/dH$ is illustrated by Fig. 4(a) for the longitudinal MR to which the AMR does not contribute. In Fig. 4(b), their temperature

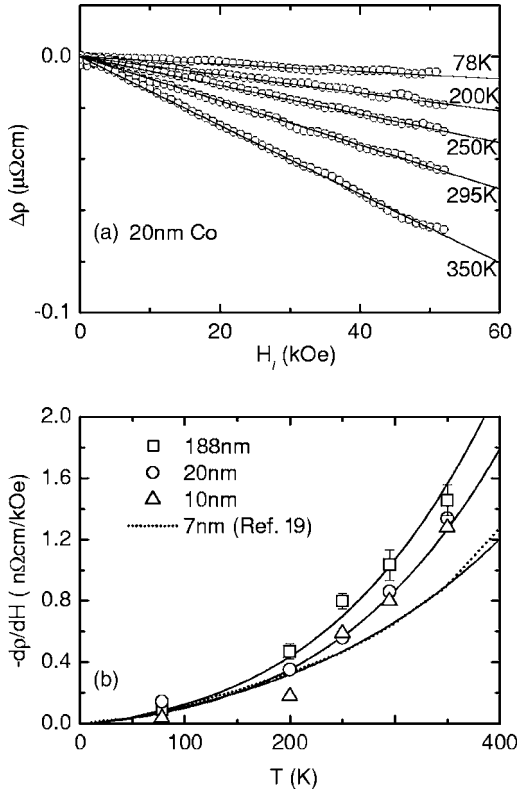


FIG. 4. (a) Longitudinal high-field MR of the 20 nm Co-film at various temperatures between 78 and 350 K. (b) Coefficient of the linear high-field MR [see panel (a) for all films vs temperature. For comparison, the dotted curve shows results for a 7 nm polycrystalline Co-film from Ref. 19, while the solid curves are fits to the prediction for scattering by spin-waves, Eq. (3).

dependence is shown for the three films under study and compared to the result for a 7 nm thin Co-film obtained by Raquet *et al.*¹⁹ These authors fitted their data to a simplified model for *sd*-scattering by magnons,²¹

$$\frac{d\rho}{dH} = AT(1 + 2d_1T^2)\ln\left(\frac{T}{T_0}\right), \quad (3)$$

where the amplitude *A* changed only little from 3 to 4 $p\Omega\text{cm}/\text{K kOe}$. Since *A* depends on the *sd*-exchange, numerical estimates are rather difficult. The coefficient $d_1 = D_1/D_0$ is determined by the ratio of the mass renormalization coefficient D_1 and the zero-temperature stiffness of the spin-waves D_0 . Independent experimental data for Co yield $d_1 = 1.57 \cdot 10^{-6} \text{ K}^{-2}$ in good agreement with calculations, and it was argued¹⁹ that d_1 might be rather insensitive to microstructural details of the films. Consequently, we fitted our data to Eq. (3) admitting (plausible) variations in the amplitude *A* and found a larger value, $d_1 = 3 \cdot 10^{-6} \text{ K}^{-2}$. We believe that the difference is related to the rather strong disorder in the present films with a residual resistance ratio (RRR) near 2 (see Fig. 2), which contrasts to RRR=27 reported by Raquet *et al.*¹⁹ for their thickest films. Hence, one may suspect that the granular disorder in our films gives rise to a stronger thermal renormalization of “the spin-wave energies.”

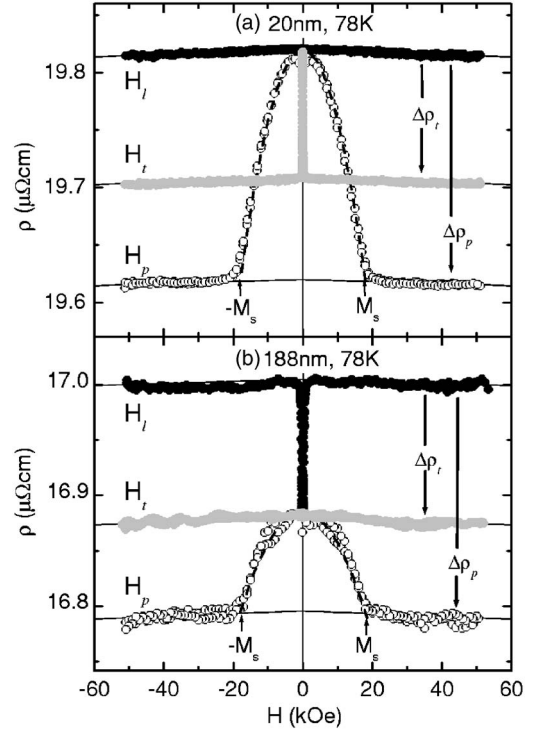


FIG. 5. High-field MR of (a) 20 nm Co- and (b) 188 nm Co-films, measured at 78 K for the three principal directions of **H** relative to the current. As for the in-plane MR, see Fig. 3(b), the quadratic decrease of the polar MR's, $\rho_p(H)$, observed for $M < M_s$ (dot curves) signals the AMR-effect also. Above technical saturation, $M(H, T) \geq M_s$, the saturation values of the transverse ($\Delta\rho_t$) and the polar ($\Delta\rho_p$) AMR's are indicated.

B. Anisotropic magnetoresistance

At low temperatures, where the spin-wave contribution vanishes, the AMR effect should prevail. This is demonstrated in Fig. 5 by the MR curves of the 20 and 188 nm films measured at $T=78$ K along the three principal directions of the field. The significant difference between the MR's of both films at smaller fields is related to the domain structure and will be discussed in Sec. IV. Here we focus on the saturated transverse and polar AMR's, $\Delta\rho_t$ and $\Delta\rho_p$, which differ significantly from each other, but do not change very much with thickness (essentially the same observation is made on the 10 nm film). This phenomenon is one of our main results: For all thicknesses, the polar AMR turns out to be about twice as large as the transverse AMR.

At first, a sizable difference between both MR's, $\Delta\rho_p > \Delta\rho_t$, has been reported by Chen and Marsocci¹⁰ for single- and poly-crystalline nickel films. They coined this feature as “geometrical size effect” (GSE) and believed that it may arise from the electronic structure inside the film material. More recently, this size-effect has also been detected on sputter-deposited 4.5–100 nm thin Permalloy films¹¹ at a low temperature, $T=5$ K. This study revealed that by raising the degree of (111)-texture in the film, $\Delta\rho_p$ was increased so that the ratio $\Delta\rho_p/\Delta\rho_t$ tended towards two. An attempt to explain this GSE by assuming an anisotropic scattering rate due to diffuse scattering at the film boundaries, however, did not provide conclusive results.¹¹

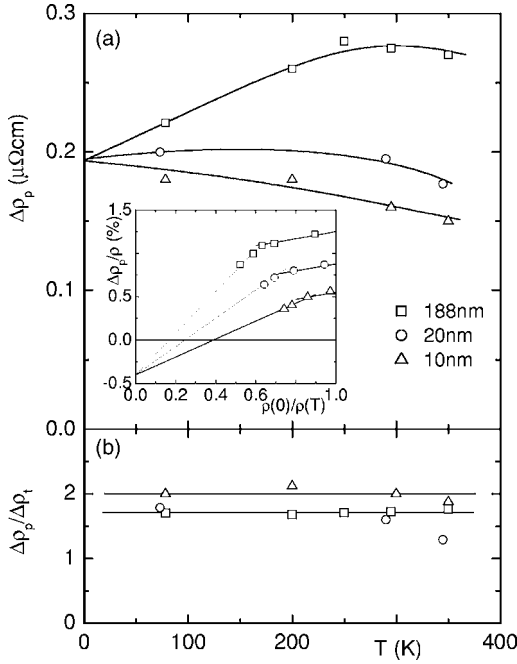


FIG. 6. Temperature dependences of (a) the saturation values of the polar magnetoresistivity $\Delta\rho_p$ and (b) of the geometrical size effect. All solid curves are guides to the eye. Inset to (a): Parker-plot analysis of $\Delta\rho_p/\rho$; the straight lines through the data indicate a common negative phonon-contribution to the MR.

In order to explore the AMR and the GSE of our Co-films in some more detail, the absolute values and the thermal behavior of both $\Delta\rho$'s are summarized in Fig. 6. Two remarkable features should be emphasized: (i) Despite different temperature variations, the MR's of all films can be extrapolated to the same value at $T=0$, as shown in Fig. 6(a) for the polar direction; (ii) Fig. 6(b) demonstrates that the GSE, i.e., the ratio of the polar and transverse AMR's, remains almost independent of temperature.

At first, we address to the AMR postponing the discussion of the GSE to the following subsection. A thickness-independence of $\Delta\rho$ itself rather than of the ratio $\Delta\rho/\rho$ has been pointed out earlier for $\text{Ni}_{0.7}\text{Co}_{0.3}$ and $\text{Ni}_{0.8}\text{Fe}_{0.2}$ alloys (see Fig. 17 of Ref. 12). For all present Co-films, $\Delta\rho_p(0) = 0.19 \mu\Omega \text{ cm}$ follows from Fig. 6(a), and we suspect that the origin of this AMR resides in the crystalline regions, to which we tentatively assigned already the bulk residual resistivity, $\rho_b(0) = 11 \mu\Omega \text{ cm}$, in Sec. II. There we determined the mean-free path, $\ell_e = 11 \text{ nm}$, which turned out to be much smaller than the grain sizes estimated from AFM images.¹⁵ Therefore, we relate the low-temperature AMR $\Delta\rho(T \rightarrow 0)$ also to the scattering within the crystalline grains and believe that the extra scattering, which enhances $\rho(0)$ in the thinner films (see inset to Fig. 2), produces a negligible AMR. In fact, a weak AMR is expected for scattering potentials with reduced symmetry, e.g., associated with phonons¹² or correlated structural disorder (grain boundaries, dislocations), because in these cases the directional symmetry-breaking effect by the magnetization \mathbf{M} via the spin-orbit interaction becomes less effective.

To discuss the effect of temperature, we employ the widely used Parker-plot²⁴ for the AMR ratio,

$$\frac{\Delta\rho(T)}{\rho(T)} = \left[\left(\frac{\Delta\rho}{\rho} \right)_d - \left(\frac{\Delta\rho}{\rho} \right)_{th} \right] \frac{\rho(0)}{\rho(T)} + \left(\frac{\Delta\rho}{\rho} \right)_{th}. \quad (4)$$

This relation is valid under the two premises: (i) the electric transport is dominated by one spin-channel, i.e., the majority channel in Co,¹⁸ and (ii) Matthiessen's rule applies for the thermal and defect scattering which has been demonstrated in Fig. 2 by the fits of $\rho(T)/\rho(0)$ to Eq. (1). Then a plot of $\Delta\rho(T)/\rho(T)$ vs $\rho(0)/\rho(T)$ can separate the thermal contribution to the AMR, $(\Delta\rho/\rho)_{th}$, from the defect one, $(\Delta\rho/\rho)_d$. Unfortunately, similar as in a previous Parker-analysis on polycrystalline Co-films,²² the data shown by the inset to Fig. 6(a) are rather consistent with two different slopes than with a single straight line, indicating a possible violation of the premise(s) for Eq. (4). Nevertheless, if we choose to fit all data from the "high-temperature" slope to a common intercept at $\rho(0)/\rho(T)=0$, we find a negative contribution $(\Delta\rho/\rho)_{th} = -0.40\%$. Such negative thermal MR has been realized early on crystalline Permalloy²⁵ and, more recently, also on polycrystalline Co-films²² and was associated with phonon-scattering rather than with magnon contributions.

C. Geometrical size effect

As a guide for discussing the GSE, we refer to Potter's work,⁵ who evaluated the AMR's of the majority and minority spin channels in polycrystalline cubic ferromagnets. He assumed an isotropic scattering potential, as it may be provided by point defects in the grains of our films. Calculating the sd -scattering rates, Potter considered the effect of the spin-orbit interaction on localized $3d$ -states ignoring the band-structure, and therefore, we can expect only a more or less qualitatively correct guidance by these results. As the majority d -orbitals of Co are fully occupied,⁹ we take only sd -scattering into the minority band into account. As shown in the Appendix, the dominant contribution to the AMR reads:

$$\frac{\Delta\rho}{\rho} = \frac{1+r}{2+r} \left\{ \frac{3\sqrt{3}}{64} \left(\frac{K_{SO}}{\epsilon_d} \right)^2 - \frac{r}{560} \left(\frac{K_{SO}}{2\epsilon_{ex}} \right)^2 \right\}. \quad (5)$$

Here $K_{SO} \approx 0.1 \text{ eV}$ measures the spin-orbit coupling energy $\mathcal{H}_{SO} = K_{SO} \mathbf{L} \cdot \mathbf{S}$. The positive contribution to Eq. (5) arises from the longitudinal part of \mathcal{H}_{SO} mixing two $3d$ -orbitals of the minority bands separated by ϵ_d near the Fermi-surface ϵ_F . The negative term is due to the nondiagonal part of \mathcal{H}_{SO} , which admixes some of the exchange-split majority states to the minority band. The parameter $r = \tau_{sd}^{-1} / \tau_{ss}^{-1}$ accounts for the different scattering rates of the conduction electrons into the $4s$ - and $3d$ -states and is mainly determined by the density of states of the $3d$ -bands at ϵ_F . Because the exchange splitting $2\epsilon_{ex}$ is significantly larger than ϵ_d , the negative majority spin contribution to the AMR may be small relative to the positive term. Taking $r \approx 10$ from a recent experiment on Co-films,¹⁸ $\Delta\rho/\rho = (3\sqrt{3}/64)(K_{SO}/\epsilon_d)^2$ follows from Eq. (5). Comparing this estimate with our result for the transverse AMR at low temperatures, $\Delta\rho_t(0)/\rho_b(0) \approx 10^{-2}$ we obtain for the effective splitting of the two unperturbed $3d$ -levels, $\epsilon_d \approx 3.0 K_{SO} \approx 0.3 \text{ eV}$. Though the value for ϵ_d would become

smaller if a finite contribution by the majority spins is considered in Eq. (5), it seems to be a reasonable result regarding the other simplifying assumptions of the theory.⁵ Here we mention the neglect of effects of the lattice potential and of the spin-orbit interaction on the Fermi-surface and on the density of states at ϵ_F ,⁵ and also of possible hybridizations between the s - and d -orbitals.⁶

Nonwithstanding the approximate nature of Potter's theory intended for an "isotropic," i.e., polycrystalline cubic ferromagnet, we will use it here as a basis to discuss the AMR of films with polar texture. To this end we recall that the AMR originates from a symmetry breaking of the $3d$ -orbitals by the magnetization \mathbf{M} via the spin-orbit coupling. The resulting anisotropic charge distribution gives rise to the scattering asymmetry of the conduction electrons into these $3d$ -states. On general grounds one may expect that a reduction of the structural symmetry and, therefore, of the scattering potential weakens the AMR, because then the effect of the magnetization on the $3d$ -orbitals becomes less effective.¹² Since the texture in the permalloy¹¹ and in our cobalt films, both perpendicular to the plane, appears to be strongly correlated with the GSE, we assume the mixing parameter in Eq. (5), $k_\alpha^2 = 3\sqrt{3}(K_{SO}/4\epsilon_\alpha)^2$, to be different for the in-plane ($\alpha=i$) and the polar ($\alpha=p$) directions of \mathbf{M} . Then Eq. (5) remains still valid for the in-plane orientations of \mathbf{M} and ignoring again the small contribution by the majority spins, we have

$$\frac{\rho_\ell - \rho_t}{\rho} = \frac{1+r}{2+r} \frac{3\sqrt{3}}{4} k_i^2. \quad (6)$$

In order to determine the effect of the film anisotropy on the polar MR, we introduce k_α^2 directly into Potters⁵ result for the perpendicular conductivity of the minority spins, $\sigma_\perp^\alpha/\sigma_0 = (3\sqrt{3}/2r) \cdot \ln[r/(1 + \frac{1}{2}rk_\alpha^2)]$. For small spin-orbit perturbations, $rk_\alpha^2 \ll 1$, the difference between the transverse and polar resistivities becomes:

$$\frac{\rho_t - \rho_p}{\rho} = \frac{1+r}{2+r} \frac{3\sqrt{3}}{4} (k_i^2 - k_p^2). \quad (7)$$

By some trivial algebra we obtain for the GSE from Eqs. (6) and (7):

$$\frac{\Delta\rho_p}{\Delta\rho_t} = 2 - \frac{k_p^2}{k_i^2}. \quad (8)$$

Hence, this simple model can explain the upper limit of two of the GSE, which emerges from our data in Fig. 6(b) and also from Fig. 6 in Ref. 11 for Permalloy films. Moreover, this model ascribes the GSE to the electronic structure, as it was suspected by Chen and Marsocci.¹⁰ Consequently, the GSE should not depend on the temperature which is fully consistent with our results depicted in Fig. 6(b).

Equation (8) also predicts that the upper limit of two is reached, when the spin-orbit mediated mixing of the $3d$ -states near ϵ_F by the polar-oriented magnetization is small compared to the mixing by the in-plane \mathbf{M} , i.e., when $k_p^2 \ll k_i^2$. This limit seems to be approached in our films, see Fig. 6(b), and also in the Permalloy films with increased

$\langle 111 \rangle$ -epitaxy (Fig. 6 of Ref. 11). These observations indicate that the mixing of the $3d$ -orbitals near ϵ_F is smallest, if \mathbf{M} is aligned parallel to the hcp- or $\langle 111 \rangle$ -epitaxy. This can be traced to the fact, that the $3d$ -orbitals have already the axial symmetry. Therefore, a magnetization aligned parallel to the symmetry axis may have only a smaller effect on the scattering probability into these states than an in-plane orientated \mathbf{M} , which breaks the symmetry of these orbitals.

It may be interesting to discuss also the effect of crystallinity on the GSE. We start with the observation that a finite GSE occurs between the limiting cases of bulk single crystals and of polycrystals with no preferred direction. While the GSE is defined to be zero in bulks single crystals,¹⁰ in "ideal" polycrystals the average over any local anisotropies yields a vanishing GSE. In passing to single-crystalline Ni-films, Chen and Marsocci,¹⁰ detected a finite GSE which, except for a high temperature, became even larger than in their polycrystalline Ni-films. This lead to the conjecture, to attribute the GSE to an unknown inherent film anisotropy acting on the electronic structure.¹⁰ Our approach to a more detailed understanding of the GSE observed here for the first time on polycrystalline Co-films, starts from the ideal polycrystalline film, to which Potters approach⁵ applies. By adding a small axial perturbation to this isotropic limit we were able to explain several essential features of the GSE. As to the origin of this axial perturbation, we suspect a relation to the film growth, and that only slightly different lattice constants for the in-plane and the polar directions (even in quasi-single crystalline films) change the electronic structure, i.e., ϵ_d supposed here. Of course, in the present example of polycrystalline Co with a built-in hcp anisotropy, intrinsic contributions of the hcp-structure cannot be excluded. However, a quantitative estimate is difficult, also because existing MR-data for bulks Co-crystals display extremely large Lorentz-MR's,^{26,27} which are several orders of magnitude larger than the AMR's in the strongly disordered films.

IV. LOW-FIELD MAGNETORESISTANCE

A. Domain structures

The formation of domains affects the MR's of the 188 nm thick film and of the thinner films, $d \leq 20$ nm, in quite different ways. The interesting features can already be realized on the large field scale of Fig. 5: (i) For $d=20$ nm Co (and also for 10 nm, not shown) both, the polar and the transverse MR's approach the field-independent longitudinal MR, ρ_ℓ , whereas the polar and the longitudinal MR's of the 188 nm film tend to the field-independent transverse resistance ρ_t . In order to provide some solid basis for a detailed discussion of these characteristic features of the domain MR's, we examine the domain structures by magnetic force microscopy (MFM).

The essential difference between the thick (188 nm) and the thinner films can be inferred from MFM images of the demagnetized states, shown in Fig. 7(a). The images have been recorded in the dynamic mode of the Q-scope which is sensitive to the polar gradient of the polar force, i.e., $\delta F_p/\delta x_p = M_p \delta^2 H_p/\delta x_p^2$. The 20 nm film consists of large, some 10 μm wide domains with in-plane magnetizations

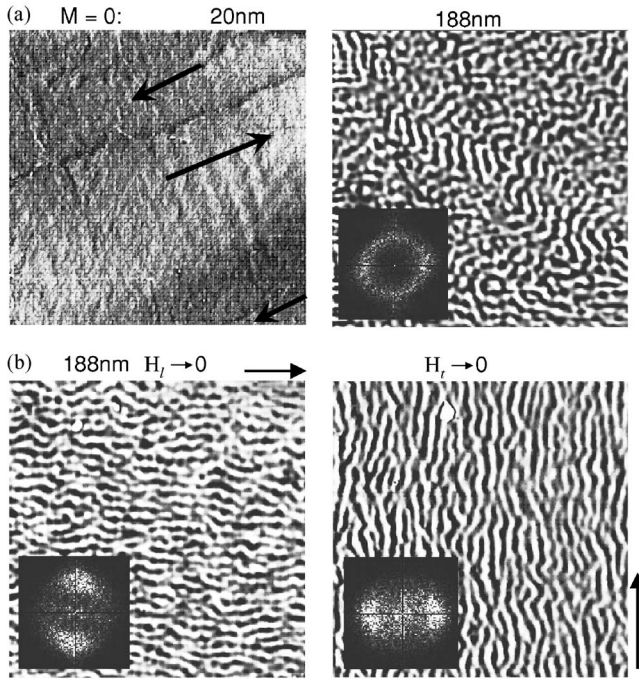


FIG. 7. Stray field images obtained by magnetic force microscopy: (a) In the demagnetized states of 188 nm Co on glass ($10 \times 10 \mu\text{m}^2$) and 20 nm Co on Si(100) ($25 \times 25 \mu\text{m}^2$). For the 20 nm film, only domains with in-plane magnetizations along the uniaxial anisotropy field \mathbf{H}_u are observed, while the 188 nm film displays a maze-structure with an out-of-plane component of \mathbf{M} . (b) In the remanent states, the 188 nm film reveals stripe domains parallel to the previously applied fields, \mathbf{H}_ℓ and \mathbf{H}_t . The insets show the Fourier-transforms which show the mean size and the directions of the stripe domains.

separated by 180° Neel walls. The domain magnetizations are oriented parallel to the uniaxial anisotropy field \mathbf{H}_u as determined by FMR. A slight longitudinal ripple of \mathbf{M} about \mathbf{H}_u is visible, which most likely arises from the polycrystallinity of the film.

In contrast, the 188 nm film exhibits a maze configuration of stripe domains with sizable polar components of the domain magnetizations. The Fourier transform of the image in Fig. 7(a) yields a mean width of the stripes, $d_D = (205 \pm 15) \text{ nm}$, being rather close to the thickness as expected for weak stripes by magnetostatic reasons.²⁸ Recently, the same observations were reported for a 195 nm thin *polycrystalline* Co-film on glass and related to a hexagonal texture perpendicular to film plane.¹³ MFM images depicted on *epitaxial* Co-films revealed a reorientation of the domain magnetization from in-plane to polar between 10 and 50 nm^{29,30} which was explained in terms of the perpendicular magnetocrystalline anisotropy of Co. These results suggest that also in our case the hcp texture, realized by the XRD (Fig. 1), generates such a crystalline anisotropy, which in the 188 nm film becomes large enough to produce a significant polar component of \mathbf{M} . Let us also recall that we supposed this texture already in the discussion of the GSE.

The other interesting property of these weak stripes is seen in Fig. 7(b). In the remanent states, stripe patterns are found aligned with the direction of the previously applied

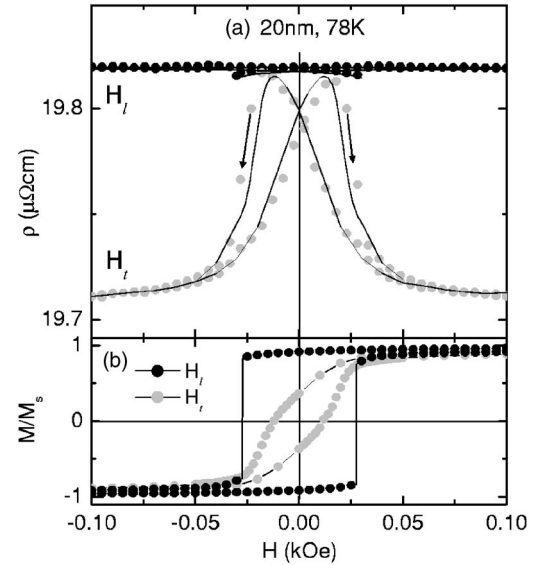


FIG. 8. (a) Low-field MR of 20 nm Co measured at 78 K for in-plane fields applied longitudinally (H_ℓ) and transversely (H_t) to the current. The solid curves are fits to the AMR effect [Eqs. (2) and (9)] using the magnetization curves $M(H_\ell)$ and $M(H_t)$ as shown in panel (b). The longitudinal field has been applied along to the growth-induced uniaxial anisotropy field $H_u = 20 \text{ Oe}$ determined by ferromagnetic resonance (Ref. 15).

fields H_ℓ or H_t . This so-called rotatable anisotropy can be attributed to the stiffness of the domain walls against deformations²⁸ and is probably supported by a pinning of the walls by local anisotropies in the granular structure. The rotatable anisotropy suggests also an “isotropic” hysteresis loop, the shape of which should be independent on the direction of the in-plane field. In fact, we do observe this feature on the 188 nm film, see Fig. 9 below, and will refer to it when discussing the MR in the domain state.

B. Anisotropic magnetoresistance

We begin with the low-field resistance of the *thin* films, exemplified by Figs. 3(a) and 5(a) for $d = 20 \text{ nm}$: Both the transverse and the polar MR's, $\rho(H_t \rightarrow 0)$ and $\rho(H_p \rightarrow 0)$, tend to the longitudinal one, $\rho(H_\ell)$. This behavior is readily explained by the fact that the resistance is measured along \mathbf{H}_u , and that at low fields the domain magnetization is also directed parallel to H_u evidenced by MFM [Fig. 7(a)]. The parabolic decrease of ρ in larger *polar* fields, $\Delta\rho(H_p < M_s) \sim -H_p^2$, was already attributed to the AMR resulting from the rotation of \mathbf{M} from an in-plane to the polar direction. Also the detailed variation of the *in-plane* MR's, shown in Fig. 8(a), can be explained by the AMR. Using the hysteresis loops $M(H_i)$ in Fig. 8(b), and assuming the relations for the angle φ in Eq. (2),

$$\cos \varphi(H_\ell) = M(H_\ell)/M_s, \quad (9a)$$

$$\sin \varphi(H_t) = M(H_t)/M_s, \quad (9b)$$

the in-plane MR can be described rather nicely. The physical

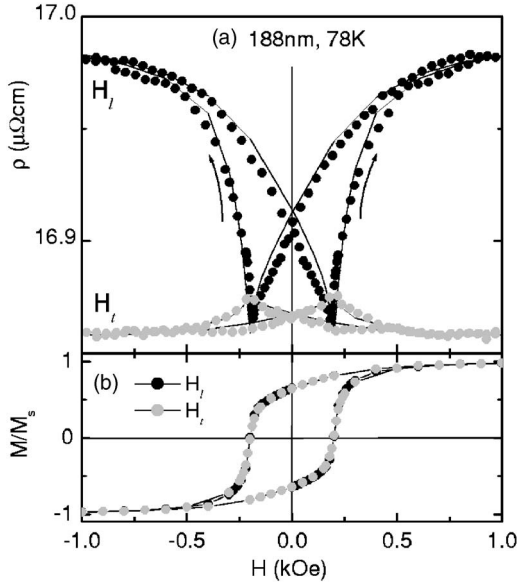


FIG. 9. (a) Low-field MR of 188 nm at 78 K in longitudinal and transverse fields. As in Fig. 7, the solid curves are fits to Eqs. (2) and (9) using the magnetization curves displayed in panel (b). Note the inversion of the longitudinal and transverse field MR-variations in comparison to the 20 nm film, shown in Fig. 8(a).

arguments for these agreements are: (i) the *longitudinal* magnetization process, $M(H_\ell)$, is due to the nucleation of 180° Neel walls [see Fig. 7(a)] at the coercive field $H_c = -H_u$ (determined by FMR), which then rapidly cross the film leaving the resistance unchanged; (ii) upon reduction of the *transverse* field, on the other hand, a longitudinal ripple of \mathbf{M} about \mathbf{H}_t appears which originates from \mathbf{H}_u (see, e.g., Chap. 5.5 of. Ref. 28). Accordingly, the components of \mathbf{M} parallel and antiparallel to the current $\mathbf{I} \parallel \mathbf{H}_u$ are growing continuously so that $\rho(H_t)$ increases until the transverse coercive field $H_c^t < H_u$ is reached. There the magnetization component along \mathbf{H}_u changes sign and increases at the expense of the ripple, so that $\rho(H_t)$ is bending back to ρ_t at larger negative fields.

A rather different behavior is displayed by the 188 nm *thick* film. Already in Fig. 5(b) we noticed that at low fields the polar and the longitudinal MR's tended to the transverse MR. As a rather unexpected feature, the transverse MR turned out to be nearly independent of the field also in the domain regime, $\rho(H_t) = \rho_t$. The detailed variation of the in-plane MR's at low fields is shown in Fig. 9(a) revealing just the opposite to the behavior of the thin films [see Fig. 8(a)]: The longitudinal MR displays a strong field dependence, while the transverse MR remains very small. These results are explained also by the AMR effect. The *in-plane* MR, shown in Fig. 9(b), is rather nicely reproduced by the solid curves which have also been calculated from Eq. (2). Again, the mean angle φ between current and magnetizations $\mathbf{M}(\mathbf{H})$ has been determined from Eq. (9) and the hysteresis loops, Fig. 9(b). As a matter of fact, we emphasize that the shape of these loops does not depend on the direction of the in-plane field ("rotatable loops"). This is consistent with the corresponding behavior of the weak stripe domains depicted by

MFM in Fig. 7(b). In contrast to the thin films, $d \leq 20$ nm, no effect by the uniaxial in-plane anisotropy field, $H_u = 15$ Oe, determined by FMR,¹⁵ is realized. The much larger coercive field, $H_c \approx 200$ Oe, stems most likely from the pinning of the stripe domain walls by the random polycrystalline anisotropy in the films.

C. Effective medium approach

Aiming at a more detailed description of the MR in the 188 nm film, again the domain structure has to be taken into account. For this purpose, we use an effective medium model, by which Rüdiger *et al.*²³ successfully interpreted the AMR of epitaxial Co-films. Introducing the volume fractions v_i for different domain species, the AMR is approximated by

$$\Delta\rho(\mathbf{H}) = \sum_{i=1}^3 v_i(\mathbf{H}) \Delta\rho_i. \quad (10)$$

Here the $\Delta\rho_i$ denote the AMR's of the corresponding domain with polar, transverse or longitudinal orientations of \mathbf{M} relative to current and film plane. By definition is $\Delta\rho_\ell = 0$ and for convenience $\Delta\rho(\mathbf{H})$ is normalized to the transverse MR, Eq. (10) takes the form

$$\frac{\Delta\rho(\mathbf{H})}{\Delta\rho_t} = v_i(\mathbf{H}) + g_s v_p(\mathbf{H}), \quad (11)$$

where $g_s = \Delta\rho_p / \Delta\rho_t$ denotes the GSE-ratio. The simplest case, $v_t = v_p = 0$ and, hence, $\Delta\rho = 0$ has been realized on the thin films at low fields.

The most interesting example is the 188 nm film, where (i) the low-field MR appears to be inverted relative to the thin films and, moreover, (ii) the transverse resistivity remains at the saturation value $\Delta\rho(H_t) = \Delta\rho_t$, even in the domain state. We will now attempt to relate these striking features displayed by Figs. 5(b) and 9 to the domain structure observed by MFM, see Fig. 7. Observation (ii) in connection with Eq. (11) implies for the concentration of polar oriented domains,

$$v_p(H_t) = \frac{1}{g_s} [1 - v_t(H_t)]. \quad (12)$$

Below the saturation field, the magnetization $M(H_t)$ and, therefore, $v_t(H_t)$, starts to decrease at the expense of a finite polar component v_p , which leads to the nucleation of stripe domains. Upon further reduction, $H_t \rightarrow 0$, the hysteresis loops display a normalized remanent magnetization $M(H_t \rightarrow 0) / M_s = 0.66(2)$, i.e., volume fraction $v_t(0) \cong 2/3$. For an estimate, we take the maximum GSE, $g_s = 2$, to find from Eq. (11) $v_p(0) = 1/6$ and by using $\sum_{i=1}^3 v_i = 1$, the same longitudinal volume fraction $v_\ell(0) = 1/6 = v_p(0)$. The agreement of both volumes implies that the nucleation of *polar* domains is accompanied by the creation of an equal amount of *longitudinally* oriented domain. Considering the square-like cross-section of the stripes following from Fig. 7(b), this result indicates that the flux extending from the polar phase is closed by the longitudinal volume $v_\ell(-H_c)$. The rotatable symmetry of the hysteresis loops implies for the longitudinal

direction also $v_p(H_\ell \rightarrow 0) = v_t(H_\ell \rightarrow 0) = 1/6$. For the longitudinal MR Eq. (10) predicts then $\Delta\rho(H_\ell \rightarrow 0)/\Delta\rho_t = 1/6 + 2 \cdot 1/6 = 1/2$, which is in close agreement with the measured value, see Fig. 9(a).

Finally, upon reduction of H_t to the coercive field, $v_p(H_t)$ increases further. The volume fraction of the polar domains at $-H_c$ can be estimated from the stripe maze of the demagnetized state, Fig. 7(a), which suggests $v_t(-H_c) = v_\ell(-H_c)$. Then, from Eq. (11) and simple algebra we obtain $v_p(-H_c) = 1/3 = v_\ell(-H_c) = v_t(-H_c)$. Thus the demagnetized state consist of equal volumes for all six possible magnetization directions, which by considering the symmetry of the stripe structure is again a plausible result. We should note that this discussion did not invoke (possible small) contributions to the MR by the Neel- and Bloch-walls in the thin and thick films, respectively. Such effects have been reported before in epitaxial Co-films^{23,31,32} with strong hcp crystalline anisotropy and quantitatively different domain dimensions.

V. SUMMARY AND CONCLUSIONS

The magnetoresistance (MR) of polycrystalline Co-films, which were characterized by XRD, FMR, SQUID-magnetometry, AFM, MFM, and temperature variable resistivity, has been investigated in fields up to 100 kOe directed along three principal directions. In the saturated state, a film anisotropic AMR was observed, for which the MR for the polar orientation of \mathbf{M} turned out to be up to twice as large as for the in-plane \mathbf{M} , similar as for the so-called geometrical size-effect (GSE).¹⁰ Basing on a correlation between the GSE and a texture detected previously on Permalloy films¹¹ and also on our Co-films by XRD, we proposed here to attribute the GSE to an anisotropic mixing of the $3d$ -levels near ϵ_F by the longitudinal part of the spin-orbit interaction, $K_{SO}L_zS_z$. By introducing this anisotropy to Potter's⁵ results for the AMR of polycrystalline cubic ferromagnets, we could explain the upper limit of two and also the temperature independence of the GSE. As a possible origin of the GSE, the electronic structure has already been conjectured in the literature,¹⁰ but not yet been worked out. Regarding the simplifying assumption of the theory,⁵ i.e., a spherical scattering potential and Fermi-surface for the final $3d$ -states, the agreements with the present data may be fortuitous. However, we believe that the texture in polycrystalline films captures the essential physics for the appearance of the GSE and that more detailed work on the GSE, considering also the effect of the spin-orbit interaction on the band-structure, may be indicated.

Based on the GSE, the hysteresis loops, and MFM images of the domain structure, the essential features MR's in the *different domain configurations* could be well described in terms of the AMR mechanism. In the demagnetized state of the thin Co-films, $d \leq 20$ nm, the magnetization is always aligned with the in-plane uniaxial anisotropy field \mathbf{H}_u so that for currents parallel to \mathbf{H}_u the MR remains zero in longitudinal fields ($\mathbf{H} \ll \mathbf{H}_u$), while it decreases for both perpendicular directions for \mathbf{H} . In the thickest film, $d = 188$ nm, on the other hand, an effective out-of-plane anisotropy arising from the hexagonal Co-texture creates rotatable stripe domains

with square cross-section, observed by MFM images and hysteresis loops. By means of an effective medium model,²³ the rather complex behavior of the MR's in the three directions of \mathbf{H} could be quantitatively explained in terms of a flux closure configuration of the magnetization components about the directions of the stripes. Approaching the coercive field, the stripes terminate in a maze configuration, and the fractional volumes of all three magnetization components proved to be equal. The surprising field-independence of the *transverse* MR originates from the squared cross-section of the stripes with transverse flux-closure and from a GSE ratio near two.

ACKNOWLEDGMENTS

The authors are indebted to the late Professor J. Appel (Hamburg) for his encouraging interest and to F. Wiekhorst for experimental support during the early steps of this work. Discussions with P. Böni (München) and D. Grundler (Hamburg) are gratefully acknowledged.

APPENDIX: THE DOMINANT AMR EFFECT

Our starting point is the reduction of the conductivity of a polycrystalline ferromagnet due to a saturated magnetization either parallel or perpendicular to the current as quoted in Eqs. 44(a) and 44(b) of Ref. 5, respectively:

$$\frac{\sigma_0 - \sigma_{\parallel}}{\sigma_0} = \frac{3\sqrt{3} N_s \beta}{2 N_d} \ell n \left[\frac{1}{16} \left(\frac{K_{SO}}{\epsilon_d} \right)^2 + \frac{N_s \beta}{N_d} \right] - \frac{1}{140} \frac{N_d \beta}{N_s} \left(\frac{K_{SO}}{2\epsilon_{ex}} \right)^2 \quad (A1)$$

$$\frac{\sigma_0 - \sigma_{\perp}}{\sigma_0} = \frac{3\sqrt{3} N_s \beta}{2 N_d} \ell n \left[\frac{1}{32} \left(\frac{K_{SO}}{\epsilon_d} \right)^2 + \frac{N_s \beta}{N_d} \right] - \frac{1}{140} \frac{N_d \beta}{N_s} \left(\frac{K_{SO}}{2\epsilon_{ex}} \right)^2. \quad (A2)$$

The terms under the logarithms in (A1) and (A2) arise from the intraband sd - and ss -scattering of the minority spins, respectively, where the sd -transitions are enabled by an intraband orbital mixing via the diagonal part of the spin-orbit interaction $\mathcal{H}_{SO}^d = K_{SO}L_zS_z$. The smaller items in $(K_{SO}/2\epsilon_{ex})^2$ result from an admixture of the exchange split $(2\epsilon_{ex})$ majority spin states to the minority band by the non-diagonal part of \mathcal{H}_{SO} . There we have neglected even smaller terms in $(K_{SO}/(2\epsilon_{ex}))^2$ from mixing between different orbital and spin states. The density of states at the Fermi-level are denoted by N_s and N_d for the s - and minority d -band. Since the dimensionless constant β measures the ratio of the squared ss - and sd -matrix elements of the (isotropic) scattering potential, the parameter $N_d/\beta N_s = r$ can be considered as the ratio of the sd - and ss -relaxation rates, $r = \tau_{sd}^{-1}/\tau_{ss}^{-1}$. The bare value $\sigma_0 = e^2 \tau_{ss} n_s / m_s$ is the conductivity of each channel in the absence of sd -scattering, which in the parallel current model is related to the mean conductivity σ by

$$\sigma = \sigma_o \frac{2+r}{1+r}. \quad (\text{A3})$$

Then, by combining (A1)–(A3) one finds for the AMR

$$\frac{\Delta\rho}{\rho} = \frac{\sigma_{\perp} - \sigma_{\parallel}}{\sigma} = \frac{1+r}{2+r} \left\{ \frac{3\sqrt{3}}{2} \frac{1}{r} \ell n \left[\frac{\frac{1}{16} \left(\frac{K_{SO}}{\epsilon_d} \right)^2 + \frac{1}{r}}{\frac{1}{32} \left(\frac{K_{SO}}{\epsilon_d} \right)^2 + \frac{1}{r}} \right] - \frac{r}{560} \left(\frac{K_{SO}}{2\epsilon_{ex}} \right)^2 \right\}. \quad (\text{A4})$$

Using a recent result for polycrystalline Co-films,¹⁸ $r \approx 10$, estimates for $K_{SO} \approx 0.1$ eV, $\epsilon_d \approx 1$ eV, and $\epsilon_{ex} \approx 2$ eV,⁹ the argument of the logarithm can be approximated by $[1 + (r/32)(K_{SO}/\epsilon_d)^2]$. As the second term of this argument is small compared to 1, we finally obtain from Eq. (A4)

$$\frac{\Delta\rho}{\rho} = \frac{1+r}{2+r} \left[\frac{3\sqrt{3}}{64} \left(\frac{K_{SO}}{\epsilon_d} \right)^2 - \frac{r}{560} \left(\frac{K_{SO}}{2\epsilon_{ex}} \right)^2 \right],$$

which is identical to Eq. (5).

- ¹D. A. Thompson, L. T. Romankiw, and A. F. Mayadas, IEEE Trans. Magn. **MAG-11**, 1039 (1975); G. Prinz, J. Magn. Magn. Mater. **200**, 57 (1999); R.-C. O'Handley, *Modern Magnetic Materials: Principles and Applications* (Wiley, New York, 2000), p. 573; edited by M. Plumer, J. van Elk, and D. Weller, *Springer Series in Surface Sciences* (Springer, Berlin, 2001), Vol. 41; S. Maekawa and T. Shinjo, *Spin Dependent Transport in Magnetic Nanostructures* (Taylor & Francis, London, 2002); B. Heinrich and J. Bland, *Applications of Nanomagnetism* (Springer-Verlag, Berlin, 2005).
- ²J. Velev, R. Sabirianov, S. Jaswal, and E. Tsymlal, Phys. Rev. Lett. **94**, 127203 (2005).
- ³J. Smit, Physica (Amsterdam) **17**, 612 (1951).
- ⁴L. Berger, Physica (Amsterdam) **30**, 1141 (1964).
- ⁵R. Potter, Phys. Rev. B **10**, 4626 (1974).
- ⁶A. Fert and I. Campbell, J. Phys. F: Met. Phys. **6**, 849 (1976).
- ⁷Y. Yao, L. Kleinman, A. H. MacDonald, J. Sinova, T. Jungwirth, D.-S. Wang, E. Wang, and Q. Niu, Phys. Rev. Lett. **92**, 037204 (2004).
- ⁸P. N. Dheer, Phys. Rev. **156**, 637 (1967).
- ⁹D. A. Papconstantopoulos, *Handbook of the Band Structure of Elemental Solids* (Plenum, New York, 1986).
- ¹⁰T. Chen and V. Marsocci, J. Appl. Phys. **43**, 1554 (1972).
- ¹¹T. G. M. Rijk, S. K. J. Lenczowski, R. Coehoorn, and W. J. M. de Jonge, Phys. Rev. B **56**, 362 (1997).
- ¹²T. McGuire and R. Potter, IEEE Trans. Magn. **MAG-11**, 1018 (1975).
- ¹³A. Kharmouche, S.-M. Chérif, A. Bourzami, A. Layadi, and G. Schmerber, J. Phys. D **37**, 2583 (2004).
- ¹⁴J. Smit, Physica (Amsterdam) **24**, 39 (1958).
- ¹⁵W. Gil, Ph.D. thesis, Fachbereich Physik, Universität Hamburg, 2004.
- ¹⁶E. Sondheimer, Adv. Phys. **1**, 1 (1952).
- ¹⁷A. F. Mayadas and M. Shatzkes, Phys. Rev. B **1**, 1382 (1970).
- ¹⁸B. A. Gurney, V. S. Speriosu, J. Nozieres, H. Lefakis, D. R. Wilhoit, and O. Need, Phys. Rev. Lett. **71**, 4023 (1993).
- ¹⁹B. Raquet, M. Viret, E. Sondergard, O. Cespedes, and R. Mamy, Phys. Rev. B **66**, 024433 (2002).
- ²⁰A. Wilson, Proc. R. Soc. London, Ser. A **167**, 580 (1938).
- ²¹D. Goodings, Phys. Rev. **132**, 542 (1963).
- ²²P. Freitas, A. Gomes, T. McGuire, and T. Plaskett, J. Magn. Magn. Mater. **83**, 113 (1990).
- ²³U. Rüdiger, J. Yu, L. Thomas, S.-S.-P. Parkin, and A.-D. Kent, Phys. Rev. B **59**, 11914 (1999).
- ²⁴R. Parker, Proc. Phys. Soc., London, Sect. A **64**, 447 (1951).
- ²⁵L. Berger and S. A. Friedberg, Phys. Rev. **165**, 670 (1968).
- ²⁶R. V. Coleman, R. C. Morris, and D. J. Sellmyer, Phys. Rev. B **8**, 317 (1973).
- ²⁷E. N. Kondorskii, O. S. Galkina, V. I. Ivanovskii, A. V. Cheremushkina, and U. T. Usarov, Sov. Phys. JETP **38**, 977 (1974); Y. Kubo, N. Shohata, H. Fujii, H. Fujiwara, and T. Okamoto, J. Phys. Soc. Jpn. **38**, 87 (1975).
- ²⁸A. Hubert and R. Schäfer, *Magnetic Domains* (Springer-Verlag, Berlin, 1998).
- ²⁹M. Hehn, S. Padovani, K. Ounadjela, and J. Bucher, Phys. Rev. B **54**, 3428 (1996).
- ³⁰M. Demand, S. Padovani, M. Hehn, K. Ounadjela, and J. Bucher, J. Magn. Magn. Mater. **247**, 147 (2002).
- ³¹J. Gregg, W. Allen, K. Ounadjela, M. Viret, M. Hehn, S. Thompson, and J. Coey, Phys. Rev. Lett. **77**, 1580 (1996).
- ³²M. Viret, D. Vignoles, D. Cole, J. Coey, W. Allen, D. Daniel, and J. Gregg, Phys. Rev. B **53**, 8464 (1996).